


 Cite this: *RSC Adv.*, 2020, 10, 3380

# Synthesis and adsorption performance of La@ZIF-8 composite metal–organic frameworks

 Junqi Li,  Haizhou Chang,\* Yuhao Li,  Qiuping Li, Kaiyuan Shen, Han Yi and Jiwei Zhang

In this study, ZIF-8 with a rhombic dodecahedron structure was prepared by a hydrothermal method. Then  $\text{La}(\text{OH})_3$  was successfully loaded onto the ZIF-8 by an immersion deposition method, to form a lanthanide-based metal–organic framework (La@ZIF-8) composites. The structure and properties of La@ZIF-8 were verified by X-ray diffraction (XRD), Fourier transform infrared spectroscopy (FT-IR), scanning electron microscopy (SEM), transmission electron microscopy (TEM), thermogravimetric analysis (TGA), and zeta potential measurements. The optimum process conditions are discussed within the materials and methods. The effects of initial phosphorus concentration, dosage, pH and contact reaction time on the phosphorus removal performance of the nanomaterial were investigated. The results indicated that La@ZIF-8 exhibited an excellent adsorption capacity ( $147.63 \text{ mg g}^{-1}$ ) and its phosphorus removal efficiency could reach as high as 99.7%. Experimental data were interpreted using different adsorption kinetic and isotherm models. The kinetic behavior conformed to the pseudo-second-order kinetic model, which indicated the chemisorption of phosphorus by La@ZIF-8. The adsorption behavior of phosphorus by La@ZIF-8 fitted well to the Langmuir isotherm model, suggesting a monolayer chemical adsorption process. The majority of the adsorbed phosphate could be desorbed by  $\text{NaOH}$  ( $2 \text{ mol L}^{-1}$ ), and the removal efficiency of the recycled La@ZIF-8 reached 90%, even after the fifth cycle. The obtained results demonstrate the great application potential of the prepared La@ZIF-8 as a fascinating adsorbent for the removal of phosphate.

 Received 15th December 2019  
 Accepted 4th January 2020

DOI: 10.1039/c9ra10548d

[rsc.li/rsc-advances](http://rsc.li/rsc-advances)

## 1. Introduction

The high usage of fertilizer in agricultural activities causes phosphorus to enter the soil and water environments.<sup>1,2</sup> It has been reported that the concentration of phosphorus in water can reach more than  $0.01\text{--}0.02 \text{ mg L}^{-1}$ , which causes the great pollution problem of eutrophication.<sup>3,4</sup> Therefore, methods for reducing the concentration of phosphorus in contaminated water have become a hot topic in environmental science.<sup>5</sup> There are many ways of reducing the concentration of phosphorus in water, such as the membrane separation method, chemical precipitation method, biological degradation method, and so on, but each of these methods is highly targeted due to its specific application scope,<sup>6,7</sup> and so it is extremely important to find a simple, low-cost method which could have a wide range of applications. Chemical adsorption could become one of the most promising phosphorus-containing waste-water treatment methods in the future because of its unique properties.<sup>8</sup> Zeolite,<sup>9,10</sup> slag,<sup>11</sup> and bentonite<sup>12</sup> are all natural adsorbents, which come from a wide range of sources but have low adsorptive

capacity. Synthetic adsorbents such as aluminium,<sup>13</sup> iron<sup>14,15</sup> oxides and hydroxides have strong adsorptive capacity, but these metal adsorbents will sink into water after adsorption and cannot be reused, resulting in material waste and sludge pollution.

A number of new adsorption materials have been developed for the removal of phosphate, as summarized recently. In particular, metal–organic frameworks (MOFs) are known to contain extremely small pores of nanometer scale,<sup>16</sup> exhibit well-ordered porous structures and chemical functionalities, have large specific surface areas, high pore volumes, adjustability of pore channels and offer directional modification of functional groups.<sup>17–19</sup> All of these characteristics suggest that MOFs are potential materials for cleaning phosphorus-contaminated water. Liu *et al.* successfully prepared La-MOFs which could adsorb phosphate from aqueous solution, but a large amount of organic solvent (DMF) was used in the synthesis method, which is very unfriendly to the environment.<sup>20</sup> Meanwhile, the water stability of MOFs poses a critical issue for their large-scale applications. Qian *et al.* developed a solution-immersion process to deposit a hydrophobic coating on the external surface of MOFs without blocking their intrinsic pores. Their research opened up a new avenue for the application of MOFs in gas adsorption in the presence of water.<sup>21</sup>

College of Science, University of Shanghai for Science and Technology, Shanghai 200093, P. R. China. E-mail: [ycchz@126.com](mailto:ycchz@126.com); [jkinglee123@163.com](mailto:jkinglee123@163.com); Tel: +86-15221936988



Furthermore, zeolitic imidazolate frameworks (ZIFs), with the same topology as zeolite sodalite, are of particular interest. ZIFs are a subclass of crystalline porous MOFs formed *via* a self-assembly approach, in which metal ions such as  $Zn^{2+}$  and  $Co^{2+}$  are linked through N atoms of deprotonated imidazolate to form unique frameworks.<sup>22,23</sup> Qian *et al.* successfully enhanced the water stability of ZIF-67 by Zn-doping during the crystallization process, which was successfully applied in water research.<sup>24</sup> Hai *et al.* first loaded Au in ZIF-8 to prepare samples with different Au contents by a solid grinding method; this prepared Au@ZIF-8 had a certain activity in gas-phase CO oxidation.<sup>25</sup> Peralta *et al.* studied the selective adsorption separation of ZIF-8 using binary mixtures of *n*-hexane and isoparaffins with different branches.<sup>26</sup> Zhang *et al.* studied the adsorption and separation performance of ZIF-8 for *n*-pentane and isopentane.<sup>27</sup>

Previous studies on ZIFs have focused on gas adsorption, but its application in water adsorption is rare. Recently, ZIF-8 was used to remove some pollutants in water and showed great potential.<sup>28</sup> Lanthanum has a strong affinity and specificity for phosphate, and is used for phosphorus removal from sewage.<sup>29</sup> Therefore, we envisaged a new composite material La@ZIF-8 that could be fabricated with different compositions of ZIFs and  $La(OH)_3$ , for application in the removal of phosphorus from wastewater. It may have great potential for future applications.

## 2. Experimental section

### 2.1 Materials

2-Methylimidazole ( $C_4H_6N_2$ ), zinc nitrate hexahydrate ( $Zn(NO_3)_2 \cdot 6H_2O$ ), triethylamine ( $C_6H_{15}N$ ), lanthanum nitrate ( $La(NO_3)_3$ ), sodium hydroxide (NaOH), sulfuric acid ( $H_2SO_4$ ), potassium dihydrogen phosphate ( $KH_2PO_4$ ), ammonium molybdate tetrahydrate ( $(NH_4)_6Mo_7O_{24} \cdot 4H_2O$ ), potassium antimony tartrate ( $C_8H_4K_2O_{12}Sb_2$ ), and ascorbic acid ( $C_6H_8O_6$ ) were purchased from Sinopharm Chemical Reagent Co., Ltd. (Shanghai, China). All chemical reagents were of analytical grade and were used without further purification.

### 2.2 Physical characterization

Scanning electron microscopy (SEM, TESCAN-VEGA3) was used to observe the surface morphologies and evaluate the chemical compositions of the samples. Raman spectroscopy (Horiba Lab-RAM HR Evolution) afforded information about the vibrational modes associated with the molecules and materials. Transmission electron microscopy (TEM, TecnaiG220) was employed to observe the dispersion of the nanoparticles. X-ray diffraction (XRD, Bruker D8 Advance) was applied to analyze the crystalline structures of the products. Thermogravimetric analysis (TGA) using a TGA-50 instrument (Shimadzu) was performed to study the thermal properties of the products. Fourier transform infrared spectroscopy (FT-IR, Nicolet 380) was performed to analyze the characteristic functional groups of the products.

### 2.3 Preparation of La@ZIF-8

**2.3.1 Synthesis of ZIF-8 precursor.** ZIF-8 was synthesized according to the method previously reported in the literature.<sup>30,31</sup>

The ZIF-8 precursor was prepared using a hydrothermal method. Firstly, 0.89 g of  $Zn(NO_3)_2 \cdot 6H_2O$  was dissolved in 40 mL deionized water with mechanical stirring for 10 minutes to form a clear solution. Meanwhile, 2-methylimidazole ( $C_4H_6N_2$ , 1.97 g) and triethylamine ( $C_6H_{15}N$ , 1 mL) were dissolved in 40 mL deionized water with mechanical stirring for 10 minutes to form a clear solution. Then, the two solutions mentioned above were transferred to a Teflon-lined autoclave and heated to 120 °C for 10 hours. Subsequently, the obtained solid product was filtrated, and washed four times with ethanol and deionized water. Finally, after drying at 80 °C for 12 hours in a vacuum environment, the ZIF-8 precursor was obtained.

**2.3.2 Synthesis of La@ZIF-8.** Samples of La@ZIF-8 were synthesized using an immersion deposition method. Firstly, 0.50 g of ZIF-8 powder was dispersed in 50 mL of 0.08 mol  $L^{-1}$   $La(NO_3)_3$  solution with ultrasonication for 5 minutes. The pH of the solution was adjusted to approx. 9 by the dropwise addition of NaOH (0.1 mol  $L^{-1}$ ), and the solution was stirred with a magnet. Then the product was washed three times with deionized water. Finally, the solid was collected by centrifugation and dried at 80 °C.

### 2.4 Static adsorption experiment

Potassium dihydrogen phosphate solution was used to simulate wastewater containing phosphorus. Each adsorption test was carried out in a 100 mL beaker containing 50 mL phosphorus solution at a concentration of 10 mg  $L^{-1}$ . First, a certain amount of La@ZIF-8 composite modified MOF material was placed in the phosphorus-containing solution, stirred and then oscillated for 12 hours at the constant temperature of 30 °C. After the adsorption test, the solution was filtered using a 0.45  $\mu m$  microporous membrane. Subsequently, the residual phosphorus concentration of the solution was determined by ammonium molybdate spectrophotometry at the wavelength of 700 nm. Three parallel experiments were conducted and the results were averaged. Finally, the effects of adsorbent dosage, adsorption time and solution pH on the phosphorus removal performance were investigated. The phosphorus removal rate ( $E$ , %) and adsorption capacity ( $Q$ , mg  $g^{-1}$ ) of the solution were calculated by the following formula:

Phosphorus removal rate:

$$E = \frac{C_o - C_e}{C_o} \times 100\% \quad (1)$$

Adsorption capacity:

$$Q = \frac{(C_o - C_e) \times V}{m} \quad (2)$$

where  $C_o$  and  $C_e$  are the initial and equilibrium concentrations of phosphate in solution (mg  $L^{-1}$ ), respectively,  $V$  represents the volume of solution (L), and  $m$  denotes the dosage of La@ZIF-8.

## 3. Results and discussion

### 3.1 Optimum preparation conditions for La@ZIF-8

Fig. 1(a) shows the effect of lanthanum nitrate concentration on the phosphorus removal rate and zeta potential of La@ZIF-8. It



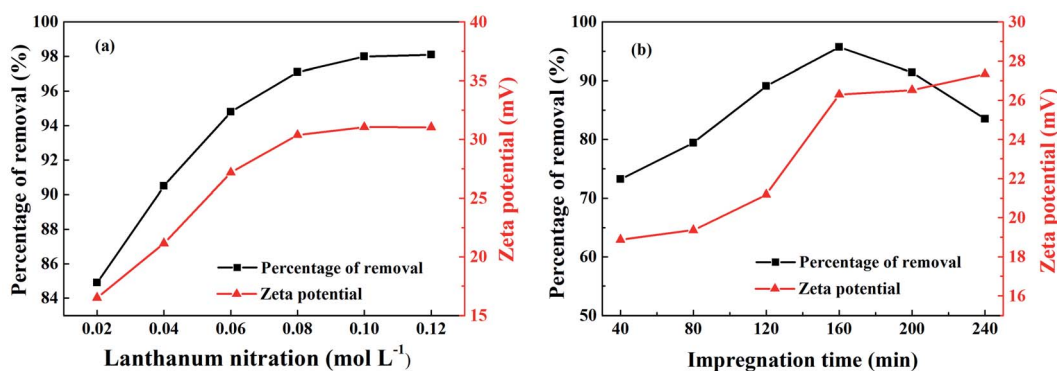


Fig. 1 Effect of different conditions on phosphorus removal rate and zeta potential of La@ZIF-8: (a) lanthanum nitrate concentration, and (b) immersion time.

can be found that both the phosphorus removal rate and zeta potential of La@ZIF-8 were boosted by increasing the lanthanum nitrate concentration. The phosphorus removal rate was as high as 98.0% at the concentration of 0.08 mol L<sup>-1</sup>, which indicates that the increase in lanthanum nitrate concentration led to the formation of more La(OH)<sub>3</sub> and a higher loading on the MOF, resulting in the augmentation of phosphorus removal rate and zeta potential. The surface of La@ZIF-8 has a high positive charge, therefore, La@ZIF-8 is more susceptible to adsorption of anions due to electrostatic interactions. These contribute to the adsorption of phosphate ions. However, when the La(OH)<sub>3</sub> load became saturated, the phosphorus removal rate no longer changed significantly as the concentration of lanthanum nitrate continued to increase.

The effect of impregnation time on phosphorus removal rate and zeta potential are shown in Fig. 1(b). When the impregnation time was less than 160 minutes, the phosphorus removal rate and zeta potential increased with time. At the impregnation time of 160 minutes, the phosphorus removal rate reached 95.7% and the zeta potential reached 26.29 mV. At this time, the system was relatively stable and the dispersion effect was optimum. However, the phosphorus removal rate showed a downward trend after the impregnation time exceeded 160 minutes. With the increase of impregnation time, the active sites on the surface of the MOF could be gradually occupied and saturated by La(OH)<sub>3</sub>. However, when the impregnation time became too long, local agglomeration of La(OH)<sub>3</sub> could occur decreasing the numbers of active sites, which reduced the phosphorus removal rate of La@ZIF-8.

Based on the abovementioned results, the optimum experimental conditions for the preparation of La@ZIF-8 composites were determined as follows: a concentration of lanthanum nitrate of 0.08 mol L<sup>-1</sup>, and an impregnation time of 160 minutes. Under the optimized conditions, La@ZIF-8 delivered both high phosphorus adsorption performance and good system stability.

### 3.2 Morphologies and microstructures of La@ZIF-8

**3.2.1 Raman study of ZIF-8.** Fig. 2 shows the Raman spectrum of ZIF-8. The illustration shows the methyl imidazole group

of ZIF-8. The majority of the vibrational peaks in the Raman spectrum are derived from the vibrations of the methyl group and imidazole rings; the corresponding peaks have been labeled in the figure. Strong bands are observed at 686 cm<sup>-1</sup>, 1146 cm<sup>-1</sup>, and 1458 cm<sup>-1</sup> in the range of 500–3200 cm<sup>-1</sup>, corresponding to the out-of-plane bending vibration of the imidazole ring, C<sub>5</sub>-N stretching vibration, and methyl bending vibration, respectively.<sup>32,33</sup> Moreover, the antisymmetric stretching vibration of the C-H in the methyl group is at about 2930 cm<sup>-1</sup>, and the C-H stretching vibration on the imidazole ring just appears at 3131 cm<sup>-1</sup>. Therefore, it can be confirmed that ZIF-8 was successfully synthesized by the reported hydrothermal method.

**3.2.2 Discussion of XRD.** The crystal structures of the synthesized powder ZIF-8 and La@ZIFs were identified with XRD and the results are displayed in Fig. 3. The XRD characterization was performed to analyze the chemical components of the as-prepared materials. The peak positions and sharp diffraction peaks of ZIF-8 crystals were indexed to 7.3°, 10.4°, 12.8°, 14.8°, 16.5°, 18.1°, 24.6°, and 26.7° in the range of 5–50°. The positions and intensities of the diffraction peaks are consistent with those reported in the literature,<sup>34–36</sup> which indicates that ZIF-8 crystals

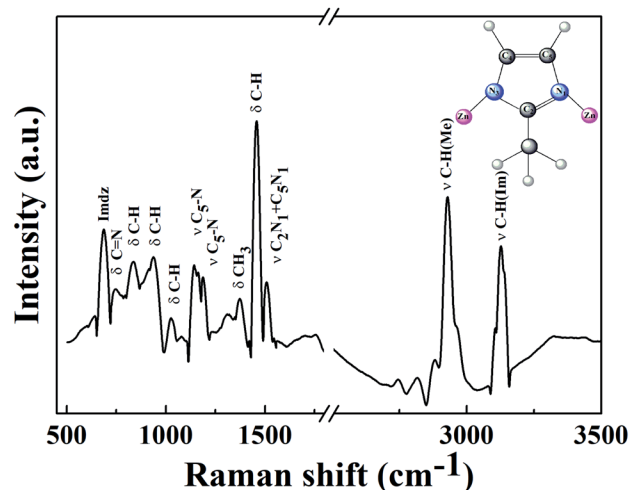


Fig. 2 Raman spectrum of ZIF-8. The inset shows the methyl imidazole group of ZIF-8.



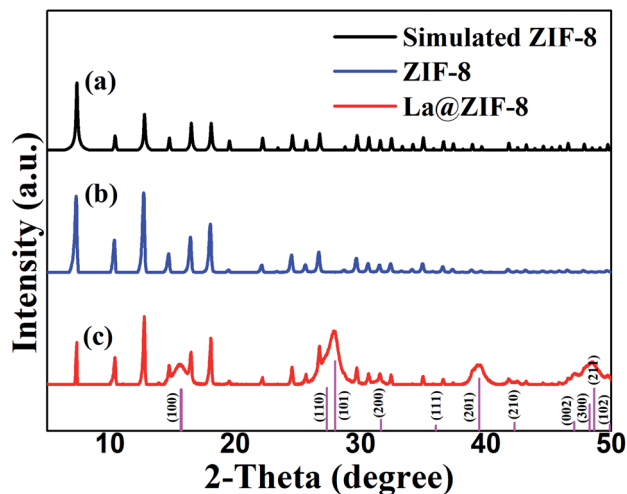


Fig. 3 XRD patterns of the simulated ZIF-8, and the as-prepared ZIF-8 and La@ZIF-8 samples.

with high purity and good crystallinity have been successfully prepared. From the comparison of (b) and (c), it can be found that the characteristic diffraction peaks of the skeleton materials were weakened after lanthanum loading, but the main characteristic peaks were basically unchanged, and ZIF-8 still had a good topological structure, which means that the coordination between  $\text{Zn}^{2+}$  and dimethylimidazole ligands was not affected at the atomic level. This indicates that the MOF was preserved after loading with lanthanum. The framework of ZIF-8 was not destroyed and no new substance was formed. The vertical line indicates the standard powder XRD peaks of lanthanum hydroxide (JCPDS 36-1481). Compared with the standard peaks, the diffraction peaks in the sample spectrum are well matched. The characteristic diffraction peaks in the XRD pattern of the sample can be attributed to the diffraction of the (100), (110), (101), (200), (111), (201), (210), (002), (211) and (102) crystal planes of  $\text{La}(\text{OH})_3$  crystals, illustrating that lanthanum hydroxide was loaded in ZIF-8.

**3.2.3 SEM & TEM images.** SEM images of the ZIF-8 and La@ZIF-8 are presented in Fig. 4(a) and (b). Fig. 4(a) reveals the homogeneous rhombic dodecahedral shape of ZIF-8, with particle sizes of around 1–2  $\mu\text{m}$ , smooth surfaces, and clear crystal surface characteristics.<sup>37</sup> Fig. 4(b) shows that the La@ZIF-8 have a rough surface, and retain a good cage structure. These results also confirm the XRD results, indicating that the main structure of the adsorption material has not changed after being loading with lanthanum hydroxide.

TEM images of the La@ZIF-8 at different magnifications are presented in Fig. 4(c) and (d). As can be seen from Fig. 4(c), the adhesion of the active component lanthanum hydroxide is not uniform, and its attachment location is relatively random. Moreover, it basically adheres to the surface of the material, indicating that attachment sites of active component exist on the surface of ZIF-8. In addition, it can be seen from Fig. 4(d) that the rod-like lanthanum hydroxide is stacked in a disorderly manner on the surface of the material and forms a porous channel structure; the adsorption performance could be improved because of this.

More evidence for crystals on the surface of La@ZIF-8 is provided through a high-resolution TEM (HR-TEM, Fig. 4(e)). The HR-TEM images correspond to the area identified by the red circle in (c). The HR-TEM results show clear lattice fringes with d-spacings of 0.32 nm and 0.56 nm belonging to the lattice fringe of the (101) and (100) planes for  $\text{La}(\text{OH})_3$ . Furthermore, the selected-area electron diffraction (SAED) pattern (Fig. 4(f)) shows clear polycrystalline diffraction rings, corresponding to the (102), (110), and (210) planes of  $\text{La}(\text{OH})_3$ .

**3.2.4 TGA.** Fig. 5 exhibits the TGA curves of La@ZIF-8 composites. It should be noted that four main weight loss stages occurred during the calcination process. The first mass loss took place below 250  $^{\circ}\text{C}$  and one sharp endothermic peak was found at 48  $^{\circ}\text{C}$ , which was ascribed to the desorption of surface water in the sample. In this process the weight loss was 5.8%. The second weight loss occurred between 250  $^{\circ}\text{C}$  and 380  $^{\circ}\text{C}$ . In the second phase, the weight loss was 6.9% and the corresponding endothermic peak presented at 300  $^{\circ}\text{C}$ . This was caused by the release of water molecules and other absorbed unreacted molecules (e.g., 2-methylimidazole) from the pore structure. Subsequently, the third stage was between 380  $^{\circ}\text{C}$  and 430  $^{\circ}\text{C}$ . With the increase of temperature, the skeleton structure of the sample collapsed and decomposed, and the structural integrity of the crystal was destroyed. In addition, La@ZIF-8 was decomposed into  $\text{ZnO}$ , resulting in a rapid mass loss of 13.1%. The last weight loss occurred above 430  $^{\circ}\text{C}$  and one sharp endothermic peak was found at 500  $^{\circ}\text{C}$ . The weight loss process was caused by the conversion of loaded lanthanum hydroxide into lanthanum oxide at high temperature. In summary, these results illustrate that the La@ZIF-8 sample has good thermal stability.

**3.2.5 FT-IR analysis.** The functional groups of powder ZIF-8, La@ZIF-8 and recycled La@ZIF-8 (P-La@ZIF-8) were confirmed by the FT-IR spectra as shown in Fig. 6. As can be seen from Fig. 6(a), the sharp absorption peak at 421  $\text{cm}^{-1}$  is related to the Zn–N stretching vibration, which is the characteristic band of ZIF-8.<sup>38</sup> In particular, the absorption peaks below 800  $\text{cm}^{-1}$  are associated with the out-of-plane imidazole ring bending, while the region of 950–1350  $\text{cm}^{-1}$  is related to in-plane ring bending.<sup>39</sup> Furthermore, a strong absorption peak appears at 1643  $\text{cm}^{-1}$ , which can be attributed to the stretching vibration of C=N. A strong and broad –OH characteristic peak appears at 3412  $\text{cm}^{-1}$  in Fig. 6(b) due to the large amount of lanthanum hydroxide on the surface of ZIF-8. A sharp bending vibration absorption band of La–O is also obvious at 640  $\text{cm}^{-1}$ , indicating that La@ZIF-8 is well loaded with lanthanum hydroxide. The FT-IR spectrum (c) of the recycled material P-La@ZIF-8 shows significant characteristic absorption peaks of La–P at 1052  $\text{cm}^{-1}$ , indicating that La@ZIF-8 could strongly adsorb phosphate ions.

### 3.3 Effect of different conditions on the adsorption of phosphate

Fig. 7(a) shows a comparison of the phosphorus removal capacity of ZIF-8 and La@ZIF-8. It can be seen that when the initial phosphorus concentration is 70  $\text{mg L}^{-1}$ , the adsorption capacities of the two are 61.37  $\text{mg g}^{-1}$  and 147.63  $\text{mg g}^{-1}$ ,



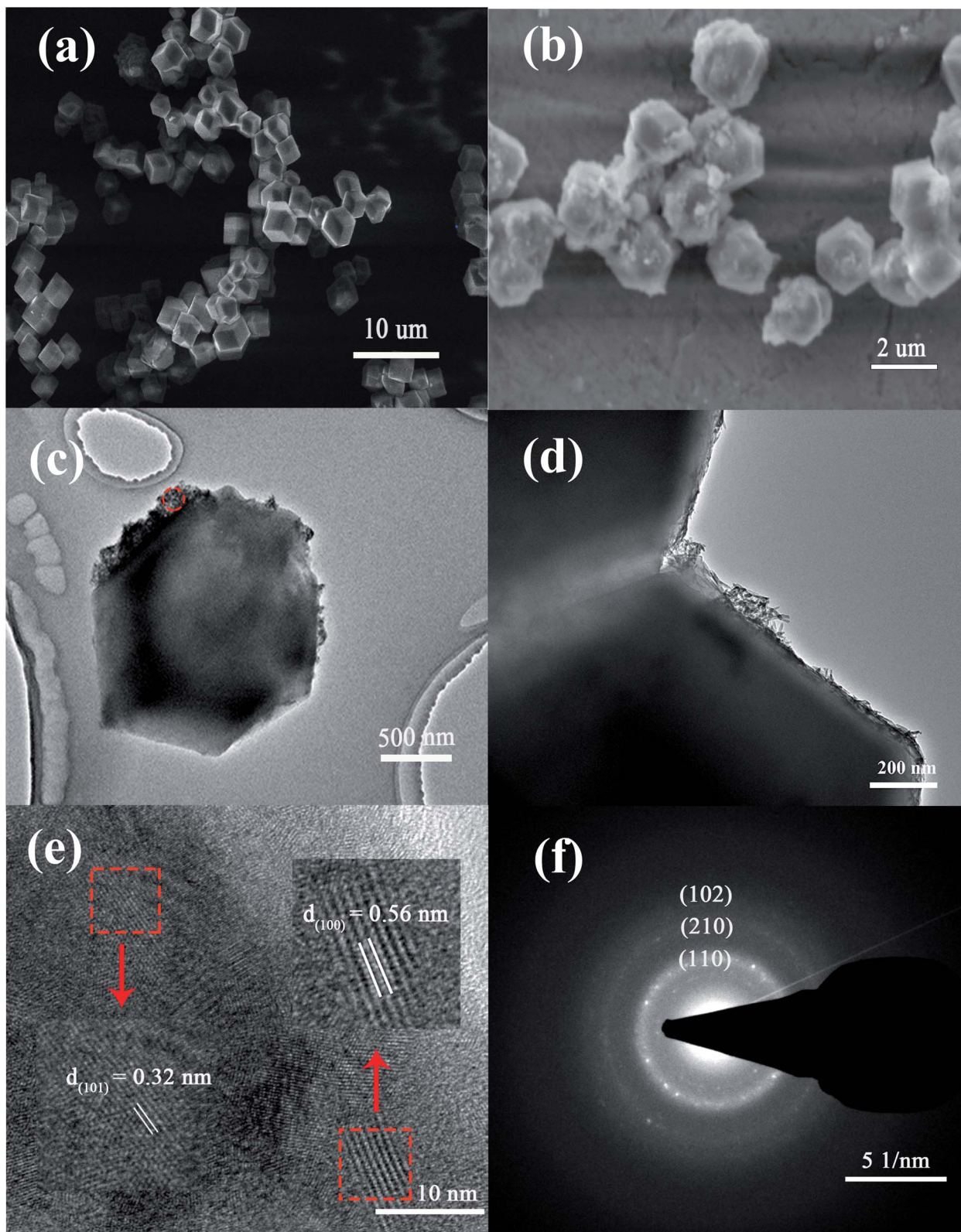


Fig. 4 (a and b) SEM images of ZIF-8 and La@ZIF-8; (c and d) TEM image of La@ZIF-8 at different magnifications; (e) HRTEM images of La(OH)<sub>3</sub> (the inner chart shows the average lattice spacing); (f) SAED pattern of La@ZIF-8.

respectively, which indicates that the loading of La(OH)<sub>3</sub> in the composites can effectively improve the adsorption capacity and plays an important role in phosphorus removal.

The effect of initial phosphorus concentration on adsorption capacity is recorded in Fig. 7(b). When the initial phosphorus concentration was low, the adsorption capacity increased



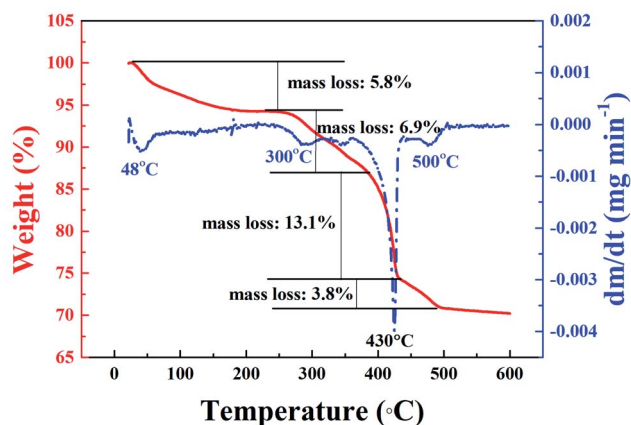


Fig. 5 TGA and DTG curves of La@ZIF-8.

rapidly as the phosphorus concentration increased. Unfortunately, when the mass concentration of phosphorus reached  $70 \text{ mg L}^{-1}$ , the adsorption capacity reached a plateau at  $147.63 \text{ mg g}^{-1}$ , after which it remained almost unchanged. This is because the adsorption sites on La@ZIF-8 composites had been gradually occupied with the increasing levels of phosphorus. However, the number of adsorption sites was limited when the dosage of La@ZIF-8 was fixed. Therefore, with increasing phosphorus content, the adsorption capacity gradually increased and then reached saturation.

The effects of La@ZIF-8 dosage on the phosphorus removal rate and adsorption capacity are shown in Fig. 7(c). Evidently, the removal efficiency of phosphate increased with the adsorbent amount from  $0.004 \text{ g L}^{-1}$  to  $0.020 \text{ g L}^{-1}$ , while the adsorption capacity declined continuously. After that, as more adsorbent was added to the solution, the removal efficiency remained at equilibrium because the number of active adsorption sites were limited at lower amounts of La@ZIF-8, leading to a lower phosphate removal efficiency. However, when the amount of adsorbent increased above  $0.020 \text{ g L}^{-1}$ , the

active adsorption sites were abundant, and the removal efficiency reached 99.7%. The adsorption capacity at the adsorbent dosage of  $0.020 \text{ g L}^{-1}$  was lower than that at  $0.016 \text{ g L}^{-1}$  because of the excess of adsorbent. Consequently, based on economical and practical considerations, the adsorbent dosage of  $0.016 \text{ g L}^{-1}$  was selected as the optimum dosage.

Fig. 7(d) shows the effect of different pH values on phosphorus removal rate. Phosphoric acid is mainly present in the form of  $\text{H}_3\text{PO}_4$ ,  $\text{H}_2\text{PO}_4^-$ ,  $\text{HPO}_4^{2-}$ , and  $\text{PO}_4^{3-}$  in solution.<sup>20</sup> Specially, the pH value affects the forms of phosphoric acid in water. At pH = 3, phosphoric acid exists mainly in the form of  $\text{H}_3\text{PO}_4$ , and the affinity between  $\text{H}_3\text{PO}_4$  and La@ZIF-8 is low, which explains why the phosphorus removal rate was low. With the increase of hydrogen ion concentration, more  $\text{H}_2\text{PO}_4^-$  is found in solution, which has a high affinity for La@ZIF-8, and the phosphorus removal rate increased accordingly. Then at pH = 6, both the adsorption capacity and the phosphorus removal rate reached their highest. However, when the pH value increased further, the phosphorus removal rate decreased because  $\text{HPO}_4^{2-}$  is the main form of phosphate in solution at pH > 7, and the affinity of hydrazine for  $\text{HPO}_4^{2-}$  is lower than that for  $\text{H}_2\text{PO}_4^-$ . At the same time, when the pH was high, the  $\text{OH}^-$  in the solution interfered with the adsorption of phosphate, which led to a decrease in adsorption capacity and phosphorus removal rate.

### 3.4 Adsorption kinetics

**3.4.1 Effect of adsorption time on adsorption capacity.** The effect of adsorption time on adsorption capacity with initial phosphorus concentrations of  $30 \text{ mg L}^{-1}$  and  $60 \text{ mg L}^{-1}$  are shown in Fig. 8. Apparently, the trend of adsorption capacity with time was basically the same under the two conditions, and La@ZIF-8 had a higher adsorption capacity for the higher concentration phosphorus solution ( $60 \text{ mg L}^{-1}$ ). When the adsorption time was less than 120 minutes, the phosphorus adsorption capacity increased rapidly with time, but after 120 minutes, the adsorption capacity did not change significantly with time.

**3.4.2 Adsorption kinetic curves.** In order to research the adsorption mechanisms and potential rate-controlling step of phosphate removal, the pseudo-first-order and pseudo-second-order kinetic models were used to describe the process of phosphate adsorption on La@ZIF-8.

The pseudo-first-order kinetic model is expressed as:<sup>40,41</sup>

$$\log(q_e - q_t) = \log q_e - \frac{k_1}{2.303} t \quad (3)$$

The pseudo-second-order kinetic model is expressed as:<sup>40,41</sup>

$$\frac{t}{q_t} = \frac{1}{k_2 q_e^2} + \frac{1}{q_e} t \quad (4)$$

where  $t$  represents the adsorption time (min),  $k_1$  is the pseudo-first-order kinetic constant (min),  $k_2$  is the pseudo-second-order kinetic constant [ $\text{g} (\text{mg min})^{-1}$ ],  $q_e$  stands for the adsorption capacity at equilibrium ( $\text{mg g}^{-1}$ ), and  $q_t$  stands for the adsorption capacity at time  $t$  ( $\text{mg g}^{-1}$ ).

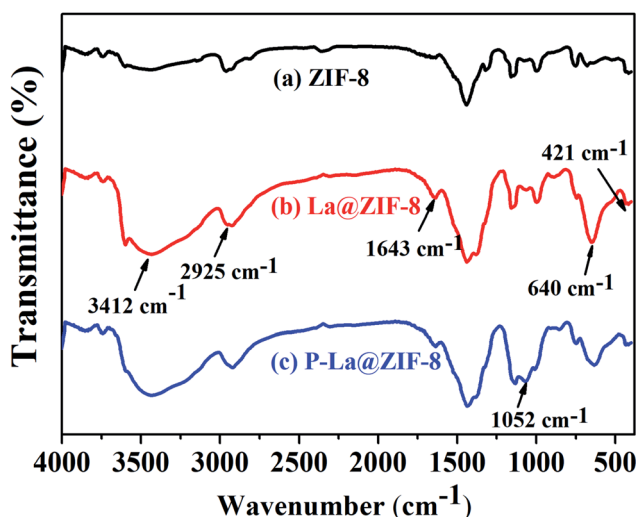


Fig. 6 FT-IR spectra of ZIF-8, La@ZIF-8 and P-La@ZIF-8.



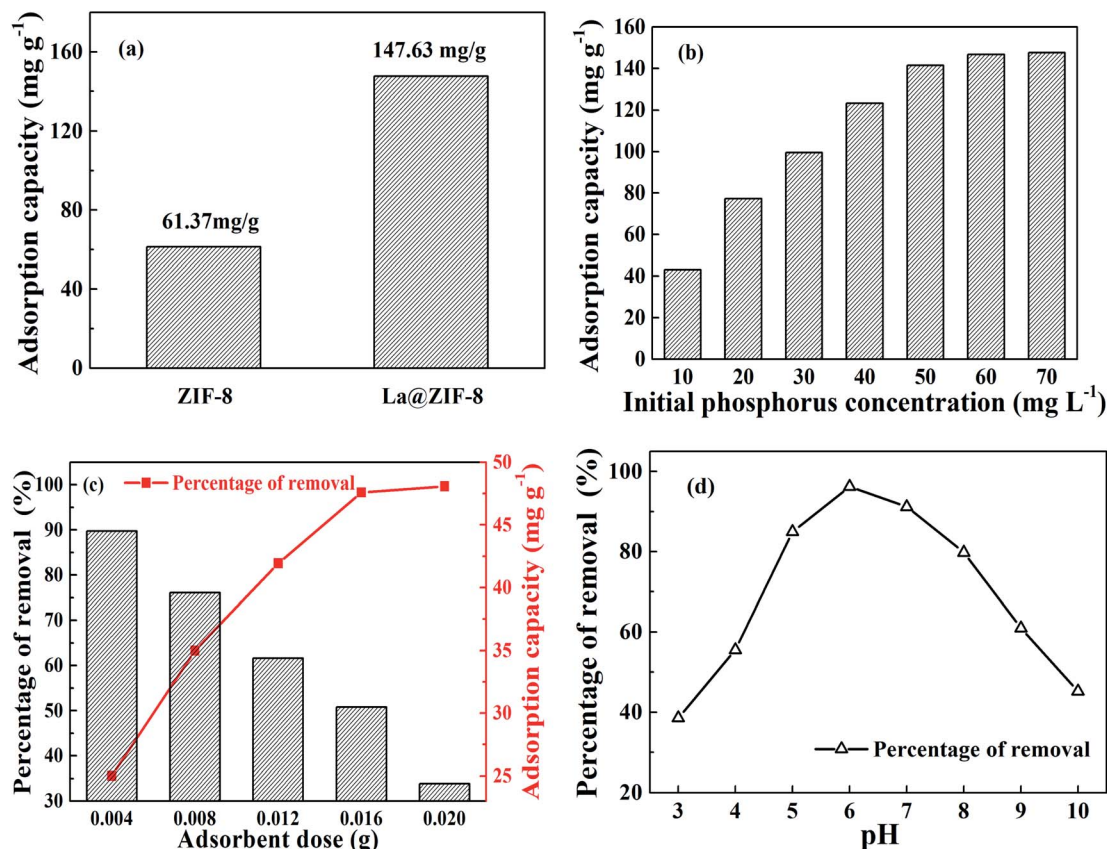


Fig. 7 Effect of different conditions on the adsorption of phosphate: (a) phosphorus removal capacity of ZIF-8 and La@ZIF-8, (b) initial phosphorus concentration, (c) adsorbent dosage, and (d) initial solution pH.

The experimental data for the phosphorus adsorption capacity of La@ZIF-8 were analyzed using the pseudo-first-order and pseudo-second-order kinetic models. Fig. 9 shows the linear relationships of the two adsorption kinetic models obtained by fitting the experimental data. Table 1 exhibits some correlative parameters of the kinetic models.

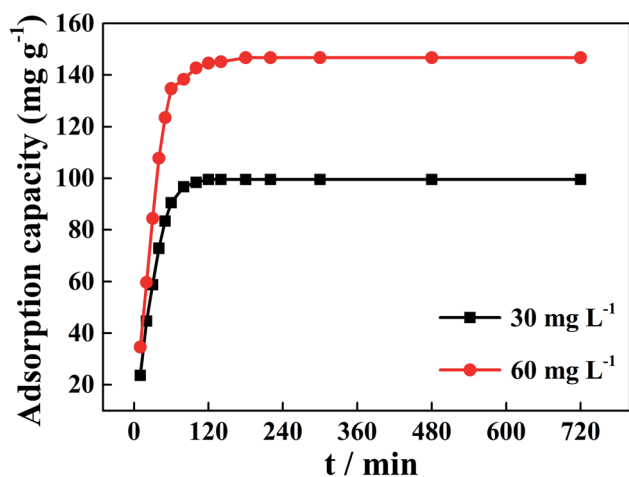


Fig. 8 Adsorption kinetics for phosphate on La@ZIF-8 at different initial phosphate concentrations.

Compared with the pseudo-first-order kinetic model, the correlation coefficients  $R^2$  of the quasi-second-order kinetic model were higher at above 0.99 for both phosphorus concentration levels. The high  $R^2$  values for the pseudo-second-order kinetic equation imply the feasibility of phosphate adsorption on La@ZIF-8. In addition, the theoretical maximum adsorption levels of 102.0 mg g<sup>-1</sup> (30 mg L<sup>-1</sup> phosphorus solution) and 151.5 mg g<sup>-1</sup> (60 mg L<sup>-1</sup> phosphorus solution), were only slightly different from the experimental values of 99.51 mg g<sup>-1</sup> and 146.70 mg g<sup>-1</sup>, respectively, further verifying the applicability of the pseudo-second-order kinetic model.<sup>18</sup> Accordingly, these results suggest that the phosphate adsorption process is chemical in nature, achieved by sharing electrons between phosphate ions and adsorbent.

### 3.5 Adsorption isotherm curve

**3.5.1 Adsorption isotherms at different temperatures.** The adsorption isotherms at different temperatures are shown in Fig. 10. Obviously, when the equilibrium concentration of the solution was low, the equilibrium adsorption amount increased rapidly, and after the concentration had reached a certain level, the rising trend of equilibrium adsorption capacity slowed down. Meanwhile, when the temperature and initial concentration were



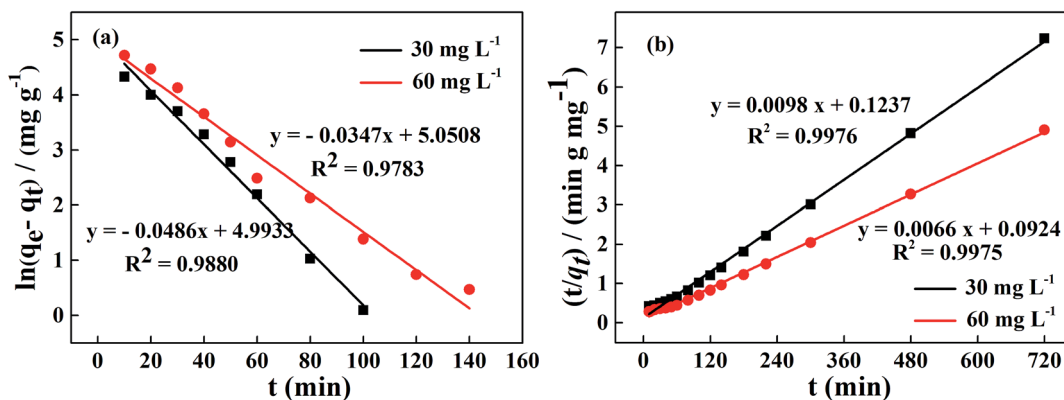


Fig. 9 Adsorption kinetics for phosphate on La@ZIF-8 at two different initial phosphate concentrations: (a) pseudo-first-order kinetic equation fitting curve, (b) pseudo-second-order kinetic equation fitting curve.

303 K and 70 mg L<sup>-1</sup>, respectively, the maximum saturated adsorption capacity reached 147.63 mg g<sup>-1</sup>.

**3.5.2 Adsorption isotherm curves.** The relationship between adsorption capacity and the equilibrium concentration of solution is expressed in the adsorption isotherm. In order to investigate the saturated adsorption capacity and adsorption isothermal properties of phosphate in La@ZIF-8 composites, the experimental data were fitted with the Langmuir and Freundlich models.

The Langmuir model describes the adsorption equilibrium of a single layer on a homogeneous surface at constant temperature.

The Langmuir isothermal model is expressed as:<sup>20,40,42</sup>

$$\frac{C_e}{q_e} = \frac{1}{K_L q_m} + \frac{C_e}{q_m} \quad (5)$$

where  $q_e$  represents the equilibrium adsorption capacity of the La@ZIF-8 composite (mg g<sup>-1</sup>),  $q_m$  represents the maximum adsorption capacity (mg g<sup>-1</sup>),  $C_e$  is the equilibrium concentration of phosphate in solution (mg L<sup>-1</sup>), and  $K_L$  stands for the Langmuir constant (L mg<sup>-1</sup>).

However, solid surfaces are often heterogeneous, with different adsorption energies at different locations, and the heat of adsorption can vary with surface coverage. Therefore, the following Freundlich empirical formula was proposed.

The Freundlich isothermal model is expressed as:<sup>20,40,42</sup>

$$\log q_e = \log K_F + \frac{1}{n} \log C_e \quad (6)$$

where  $K_F$  stands for the Freundlich constant (mg g<sup>-1</sup>), and  $n$  indicates sorption favorability.

The linear fitting of the Langmuir model is shown in Fig. 11(a). Table 2 exhibits some correlative parameters of the isotherm models. Compared with the Freundlich model as displayed in Fig. 11(b), the correlation coefficients of the Langmuir model were greater than more than 0.9800, which indicates that the Langmuir model could better describe the phosphorus adsorption process of La@ZIF-8. Furthermore, in this model, the adsorption capacity of La@ZIF-8 reached 151.51 mg g<sup>-1</sup> at 303 K, which is close to the experimental determination of 147.63 mg g<sup>-1</sup>. This indicates that the

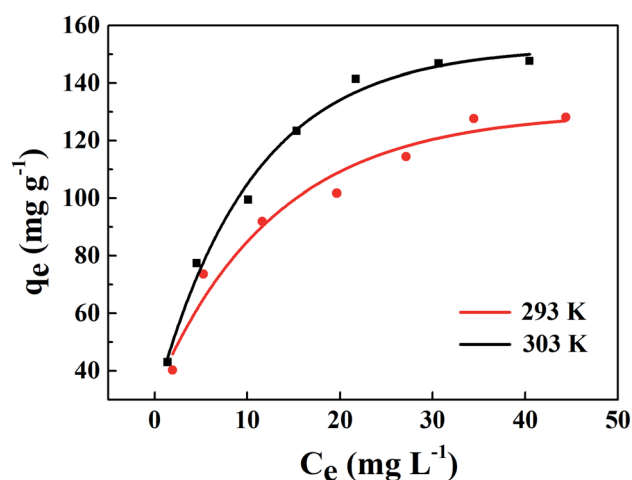


Fig. 10 Adsorption isotherms of phosphate on La@ZIF-8 at different temperatures.

Table 1 Kinetic model parameters for the adsorptive removal of phosphate using La@ZIF-8 composites

$c_0 / (\text{mg L}^{-1})$	$q_{e,\text{exp}} / (\text{mg g}^{-1})$	Pseudo-first-order kinetic model			Pseudo-second-order kinetic model		
		$q_e / (\text{mg g}^{-1})$	$k_1 / (\text{min})$	$R^2$	$q_e / (\text{mg g}^{-1})$	$k_2 / [g (\text{mg min})^{-1}]$	$R^2$
30	99.51	147.42	0.0486	0.9880	102.04	$7.764 \times 10^{-4}$	0.9976
60	146.70	156.16	0.0347	0.9783	151.52	$4.714 \times 10^{-4}$	0.9975



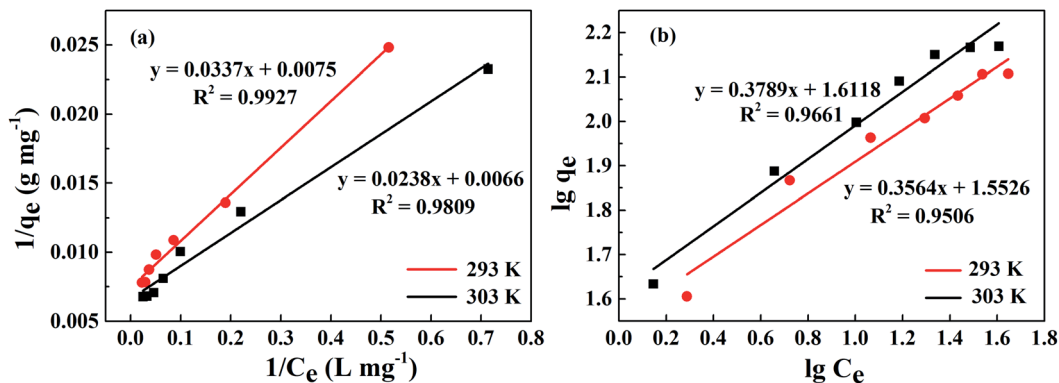


Fig. 11 Adsorption isotherms of phosphate on La@ZIF-8 at different temperatures: (a) Langmuir equation fitting curve, (b) Freundlich equation fitting curve.

Langmuir model can be used to describe the adsorption behavior of La@ZIF-8 for phosphate. Accordingly, the results reveal that phosphate adsorbs as a homogeneous monolayer on La@ZIF-8.

### 3.6 The regeneration of adsorbent

In actual application, the re-usability of adsorbents is an important characteristic. Therefore, five experiments of adsorption-desorption recycling using simulated wastewater containing  $5 \text{ mg L}^{-1}$  phosphorus were carried out. NaOH standard solution ( $1.0 \text{ mol L}^{-1}$ ) was used as the eluent and stirred with the composite at room temperature for 12 hours.

Five cycles of adsorption-desorption of phosphate by La@ZIF-8 are shown in Fig. 12. Over the five cycles, the phosphorus removal efficiency decreased slightly with the number of recycling times, which might be caused by the loss of materials in the recycling process. However, the desorption efficiency was maintained at more than 90%, indicating that La@ZIF-8 composites have good re-usability.

### 3.7 Adsorption mechanisms

Phosphoric acid is mainly present in solution in the forms of  $\text{H}_3\text{PO}_4$ ,  $\text{H}_2\text{PO}_4^-$ ,  $\text{HPO}_4^{2-}$ , and  $\text{PO}_4^{3-}$  depending on the pH value of the solution. Under strongly acidic conditions, the main form of phosphate in solution is  $\text{H}_3\text{PO}_4$ . The binding ability of  $\text{H}_3\text{PO}_4$  to La@ZIF-8 composite is weak. Under weakly acid conditions,  $\text{H}_2\text{PO}_4^-$  is the major species in solution. On the one hand, due to the electrostatic attraction between  $\text{La}^{3+}$  and  $\text{H}_2\text{PO}_4^-$ ,  $\text{La}^{3+}$  in the composite can easily form a complex with  $\text{H}_2\text{PO}_4^-$ , which improves the phosphate adsorption

capacity of the composite. On the other hand,  $\text{La}^{3+}$  binds a large amount of  $\text{OH}^-$ . The  $\text{OH}^-$  in the ZIF-8 can undergo ligand exchange with the phosphate ions in the solution, and the phosphate ions are therefore adsorbed on the surface, further enhancing the adsorption performance of the La@ZIF-8. However, with the increase of pH, the increased concentration of  $\text{OH}^-$  makes the composite surface negatively charged, and the adsorption of phosphate is disadvantageous due to the electrostatic repulsion between the surface of the La@ZIF-8 and the phosphate ions. In addition, the ligand exchange further increases the pH value of the solution, which adversely affects the adsorption of phosphate.

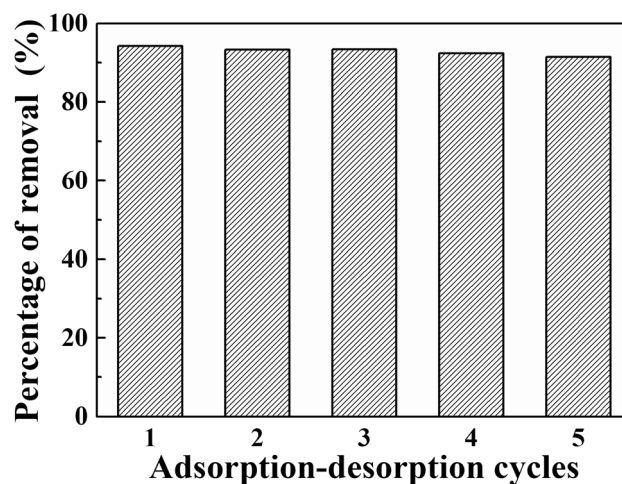


Fig. 12 Reusability of La@ZIF-8 for the adsorptive removal of phosphate.

Table 2 Langmuir and Freundlich adsorption isotherm fitting parameters for phosphate on La@ZIF-8 composites

Temperature/(K)	$q_{e,\text{exp}}/(\text{mg g}^{-1})$	Langmuir model			Freundlich model		
		$q_m/(\text{mg g}^{-1})$	$K_L/(\text{L mg}^{-1})$	R2	$n/(\text{L mg}^{-1})$	$K_F/(\text{mg g}^{-1})$	$R^2$
293	137.20	133.33	0.22	0.9927	2.81	35.69	0.9506
303	147.63	151.51	0.28	0.9809	2.64	41.50	0.9661



## 4. Conclusions

In this study, the prepared La@ZIF-8 composites were used as adsorbents for the removal of phosphate. Through the study of phosphorus removal rate and zeta potential of La@ZIF-8 composites, the optimum synthesis conditions for La@ZIF-8 were obtained. Moreover, several primary experimental parameters (such as adsorbent dosage, pH, and regeneration ability, etc.) were investigated in detail. The results showed that La@ZIF-8 has high adsorption efficiency for phosphate pollutants and exhibits the most efficient phosphate removal performance at pH = 6.0. In addition, the adsorption kinetics of the La@ZIF-8 composite for phosphorus in solution accorded with the pseudo-second-order kinetic model. Compared with the Freundlich model, the Langmuir model more accurately described the adsorption behavior of La@ZIF-8 for phosphate. By considering the adsorption mechanism, it was found that not only electrostatic attractions, but also ligand exchange reactions between phosphate ions and La@ZIF-8 facilitate adsorption. Finally, NaOH solution was selected as the elution agent for the regeneration of the sorbents. After five adsorption-desorption cycles, the capacities for the regenerated sorbents were still higher than 90%. Naturally, these advantages make it possible for La@ZIF-8 to become one of the most effective and promising adsorbent materials for phosphate in actual applications.

## Conflicts of interest

We declare that we do not have any commercial or associative interest that represents a conflict of interest in connection with the work submitted.

## Acknowledgements

This work was financially supported by the National Natural Science Foundation of China (Grant No. 21276156).

## References

- W. Guo, Y. Fu, B. Ruan, H. Ge and N. Zhao, *Ecol. Indic.*, 2014, **36**, 254–261.
- W. Zhang, X. Jin, D. Liu, C. Lang and B. Shan, *J. Environ. Sci.*, 2017, **5**, 41–48.
- S. C. Schneider, M. Cara, T. E. Eriksen, B. Budzakovska Goreska, A. Imeri, L. Kupe, T. Lokoska, S. Patceva, S. Trajanovska and S. Trajanovski, *Limnologia*, 2014, **44**, 90–97.
- Z. K. Ni, S. R. Wang and Y. M. Wang, *Environ. Pollut.*, 2016, **219**, 537–544.
- L. W. Ngatia, Y. P. Hsieh, D. Nemours, R. Fu and R. W. Taylor, *Chemosphere*, 2017, **180**, 201–211.
- L. A. Wendling, P. Blomberg, T. Sarlin, O. Priha and M. Arnold, *Appl. Geochem.*, 2013, **37**, 157–169.
- H. C. Guo and T. Ouyang, *J. Xiamen Univ., Nat. Sci.*, 2006, **45**, 540–544.
- Y. Yao, B. Gao, M. Inyang, A. R. Zimmerman, X. D. Cao, P. Pullammanappallil and L. Y. Yang, *J. Hazard. Mater.*, 2011, **190**, 501–507.
- J. W. Lin, Y. Liu and Y. H. Yan, *J. Environ. Eng.*, 2010, **4**, 575–580.
- Q. P. Cheng, H. X. Li, Y. L. Xu, S. Chen, Y. H. Liao, F. Deng and J. F. Li, *PLoS One*, 2017, **12**, 1–12.
- B. Kostura, H. Kulveitová and J. Lesko, *Water Res.*, 2005, **39**, 1795–1802.
- J. H. Xu, Y. M. Li and Y. F. Xie, *Non-Metallic Mines*, 2006, **5**, 44–46.
- Y. P. Yan, F. Liu, W. Li, F. Liu, X. H. Feng and D. L. Sparks, *Eur. J. Soil Sci.*, 2014, **65**, 308–317.
- C. Jiang, L. Y. Jia, Y. L. He, B. Zhang, G. Kirumba and J. Xie, *J. Colloid Interface Sci.*, 2013, **402**, 246–252.
- Z. L. Shi, F. M. Liu and S. H. Yao, *N. Carbon Mater.*, 2011, **26**, 299–306.
- K. S. Park, Z. Ni, A. P. Côté, J. Y. Choi, R. Huang, F. J. Uriberomo, H. K. Chae, M. O'Keeffe and O. M. Yaghi, *Proc. Natl. Acad. Sci. U. S. A.*, 2006, **103**, 10186–10191.
- V. M. Aceituno Melgar, H. Ahn, J. Kim and M. R. Othman, *J. Ind. Eng. Chem.*, 2015, **21**, 575–579.
- Y. Y. Liu, Z. Ng, E. A. Khan, H. K. Jeong, C. Ching and Z. P. Lai, *Microporous Mesoporous Mater.*, 2009, **118**, 296–301.
- C. S. Wu, Z. H. Xiong, C. Li and J. M. Zhang, *RSC Adv.*, 2015, **5**, 82127–82137.
- H. Liu, W. Guo, Z. Liu, X. Li and R. Wang, *RSC Adv.*, 2016, **6**, 105282–105287.
- X. K. Qian, F. X. Sun, J. Sun, H. Wu, F. Xiao, X. Y. Wu and G. S. Zhu, *Nanoscale*, 2017, **9**, 2003–2008.
- N. T. T. Nguyen, H. Furukawa, F. Gándara, H. T. Nguyen, K. E. Cordova and O. M. Yaghi, *Angew. Chem., Int. Ed.*, 2015, **53**, 10645–10648.
- H. Hayashi, A. P. Caté, H. Furukawa, M. O'Keeffe and O. M. Yaghi, *Nat. Mater.*, 2007, **6**, 501–506.
- X. K. Qian, Q. B. Ren, X. F. Wu, J. Sun, H. Y. Wu and J. Lei, *ChemistrySelect*, 2018, **3**, 657–661.
- H. L. Jiang, B. Liu, T. Akita, M. Haruta, H. Sakurai and Q. Xu, *J. Am. Chem. Soc.*, 2009, **131**, 11302–11303.
- D. Peralta, G. Chaplais, A. Simon-Masseron, K. Barthelet and G. D. Pirngruber, *Ind. Eng. Chem. Res.*, 2012, **51**, 4692–4702.
- L. Zhang, G. Qian, Z. J. Liu, Q. Cui, H. Y. Wang and H. Q. Yao, *Sep. Purif. Technol.*, 2015, **156**, 472–479.
- Y. H. Wang, S. G. Jin, Q. Y. Wang, G. H. Lu, J. J. Jiang and D. R. Zhu, *J. Chromatogr. A*, 2013, **1291**, 27–32.
- Y. W. Cui, J. Li and Z. F. Du, *J. Rare Earths*, 2016, **34**, 460–467.
- S. R. Venna, J. B. Jasinski and M. A. Carreon, *J. Am. Chem. Soc.*, 2010, **132**, 18030–18033.
- N. K. Demir, B. Topuz, L. Yilmaz and H. Kalipcilar, *Microporous Mesoporous Mater.*, 2014, **198**, 291–300.
- D. A. Carter and J. E. Pemberton, *J. Raman Spectrosc.*, 2015, **28**, 939–946.
- C. J. Mao, X. W. Hu, J. M. Song, H. L. Niu and S. Y. Zhang, *Crystengcomm*, 2012, **14**, 6823–6826.
- T. T. Xing, Y. B. Lou, Q. L. Bao and J. X. Chen, *Crystengcomm*, 2014, **16**, 8994–9000.



- 35 H. Bux, A. Feldhoff, J. Cravillon, M. Wiebcke, Y. S. Li and J. Caro, *Chem. Mater.*, 2011, **23**, 2262–2269.
- 36 S. R. Venna and M. A. Carreon, *J. Am. Chem. Soc.*, 2010, **132**, 76–78.
- 37 N. T. Tran, J. Kim and M. R. Othman, *Microporous Mesoporous Mater.*, 2019, **285**, 178–184.
- 38 E. Shamsaei, Z. X. Low, X. Lin, A. Mayahi, H. Liu, X. Zhang, J. Z. Liu and H. Wang, *Chem. Commun.*, 2015, **51**, 11474–11477.
- 39 Y. Hu, H. Kazemian, S. Rohani, Y. N. Huang and Y. Song, *Chem. Commun.*, 2011, **47**, 12694–12696.
- 40 J. Lalley, C. Han, X. Li, D. D. Dionysiou and M. N. Nadagouda, *Chem. Eng. J.*, 2016, **284**, 1386–1396.
- 41 A. Sari and M. Tuzen, *J. Hazard. Mater.*, 2008, **157**, 448–454.
- 42 A. Sari and M. Tuzen, *J. Hazard. Mater.*, 2009, **171**, 973–979.

